



Boron doping activate strong metal-support interaction for electrocatalytic hydrogen evolution reaction in full pH range

Qingping Yu ^a, Yixin Fu ^{a,b}, Jiarui Zhao ^c, Bin Li ^a, Xinpeng Wang ^a, Xiaobin Liu ^{a,b,*}, Lei Wang ^{a,b,**}

^a Key Laboratory of Eco-chemical Engineering, International Science and Technology Cooperation Base of Eco-chemical Engineering and Green Manufacturing, College of Chemistry and Molecular Engineering, Qingdao University of Science and Technology, Qingdao 266042, PR China

^b College of Environment and Safety Engineering, Qingdao University of Science and Technology, Qingdao 266042, PR China

^c College of Chemical Engineering, Qingdao University of Science and Technology, Qingdao 266042, PR China



ARTICLE INFO

Keywords:

Hydrogen evolution reaction
Metal-support interaction
Boron doping
Electrocatalysis

ABSTRACT

Developing rhodium-based electrocatalysts with strong metal-support interaction (SMSI) is crucial for hydrogen evolution reaction (HER) in full pH range, but it is still challenging. In this work, a boron doping strategy is proposed to activate the SMSI of ultra-small Rh nanoparticles encapsulated by N-doped carbon matrix (B-Rh@NC). Density functional theory (DFT) reveals that boron doping can regulate the electronic structure and the water adsorption energy, further boosting the HER activity. Consequently, the as-prepared B-Rh@NC nanospheres possess Pt-like activity for HER with low overpotentials in 1.0 M KOH ($\eta_{10} = 26$ mV), 0.5 M H₂SO₄ ($\eta_{10} = 43$ mV), and 1.0 M PBS ($\eta_{10} = 70$ mV), as well as outstanding stability. This work opens up a new way to construct remarkable pH-universal electrocatalysts.

1. Introduction

Hydrogen is an efficient alternative to fossil fuels owing to the high energy density (~ 142 MJ kg⁻¹) and environmental friendliness, and electrocatalytic water splitting is a promising strategy to produce hydrogen [1–7]. Pt-based catalysts are the admitted benchmark of hydrogen evolution reaction (HER) in acid electrolyte, but it displays sluggish kinetics of HER in alkaline or neutral solution [8]. Considering the inevitable variation in proton concentration and practical application for hydrogen production, ideal electrocatalyst should display excellent performance in different solutions, such as acidic solution for proton exchange membrane (PEM) electrolyzers, alkali or neutral media for anion exchange membrane (AEM) electrolyzers [9–12]. Therefore, developing catalyst with excellent HER activity even exceeding Pt-based catalysts in a wide pH range is urgently needed.

Over the past decades, researchers have been devoted to design pH-universal rhodium based electrocatalysts for HER [13–21], but still facing two main challenges. On the one side, the corrosion of Rh active sites in extreme harsh pH electrolyte is the main reason for the restricted

activity and inferior durability of electrocatalyst [22,23]. It is an effective strategy to stabilize the catalyst via encapsulating the metal catalyst by a carbon matrix with strong metal-support interaction (SMSI). In addition, the SMSI can be activated and enhanced by heterogeneous element doping, which possess strong modulation ability for chemisorption of reaction intermediates on the electrocatalyst surface [24]. On the other side, the speed and limit of the electrochemical reaction largely depend on the specific surface area and particle size of the catalysts [25,26]. The catalyst with high surface area and small particle size (lower than 10 nm) will shorten the reaction path, leading to accelerated electron/mass transport during HER process. What's more, the electronic/surface structure and metal-support interaction of the electrocatalyst change obviously with the decrease of particle size [27]. Therefore, a universal approach to design ultra-small Rh-based electrocatalyst with enhanced SMSI is highly desired.

Based on the above considerations, we report a facile boron doping strategy to activate the SMSI of ultra-small Rh@NC nanoparticles. Density functional theory (DFT) reveals that boron doping can regulate the electronic structure and the water adsorption energy, further

* Corresponding author at: Key Laboratory of Eco-chemical Engineering, International Science and Technology Cooperation Base of Eco-chemical Engineering and Green Manufacturing, College of Chemistry and Molecular Engineering, Qingdao University of Science and Technology, Qingdao 266042, PR China.

** Correspondence to: Qingdao University of Science and Technology, Qingdao 266042, PR China.

E-mail addresses: liuxb@qust.edu.cn (X. Liu), inorchemwl@126.com (L. Wang).

boosting the HER activity. The optimized B-Rh@NC possess Pt-like HER activity with low overpotentials of 26, 43, and 70 mV to drive 10 mA cm⁻² in 1.0 M KOH, 0.5 M H₂SO₄, and 1.0 M PBS, respectively, and display a better cycling durability in comparison with commercial Pt/C. Moreover, renewable energies (solar and thermal impetus) can efficiently drive the electrolysis of water, verifying the practical value of B-Rh@NC as cathode for hydrogen production.

2. Experimental

2.1. Synthesis of Rh/B-blended nanospheres

In the synthesis of Rh/B-blended nanospheres, a solution (60 mL) of aniline (0.38 g), pyrrole (0.28 g), and Triton X-100 (0.08 g) were mixed under stirring for 0.5 h and ultrasonication for another 0.5 h and then precooled at 0 °C for 0.5 h. After that, aqueous solution (20 mL) of (NH₄)₂S₂O₈ (1.91 g) precooled at 0 °C for 0.5 h was added to the above surfactant solution. The resulting solution was thoroughly stirred to acquire a homogeneous solution and maintained at 0 °C for 12 h for

polymerization reaction. Afterwards, the as-obtained dark brown product was washed with deionized water and ethanol for several times, and then the as-obtained dark brown product (2 g) re-dispersed into aqueous solution (20 mL) of RhCl₃·3 H₂O (0.26 g) and H₃BO₃ (0.25 g) with the mole ratio of 1:4 under ultrasonication for 0.5 h. And then dried whole night at 60 °C, forming Rh/B-blended nanospheres.

2.2. Synthesis of B-Rh@NC nanospheres

The as-prepared 0.3 g of Rh/B-blended nanospheres were annealed at 800 °C (5 °C min⁻¹) for 4 h under Ar gas flow in the tube furnace. This stage involves the removal of Triton X-100 surfactant, the collapse of the carbon framework, the diffusion of H₃BO₃ into carbon matrix, and the formation of new phase embedded in carbon layers in nanoscale. After cooling down to room temperature, the obtained black powder was washed with distilled water and ethanol and then dried in vacuum. This facile one-step pyrolysis process resulted in the final B-Rh@NC nanospheres. To further understand the interplay between the structures and electrocatalytic activities of B-Rh@NC nanospheres, two additional

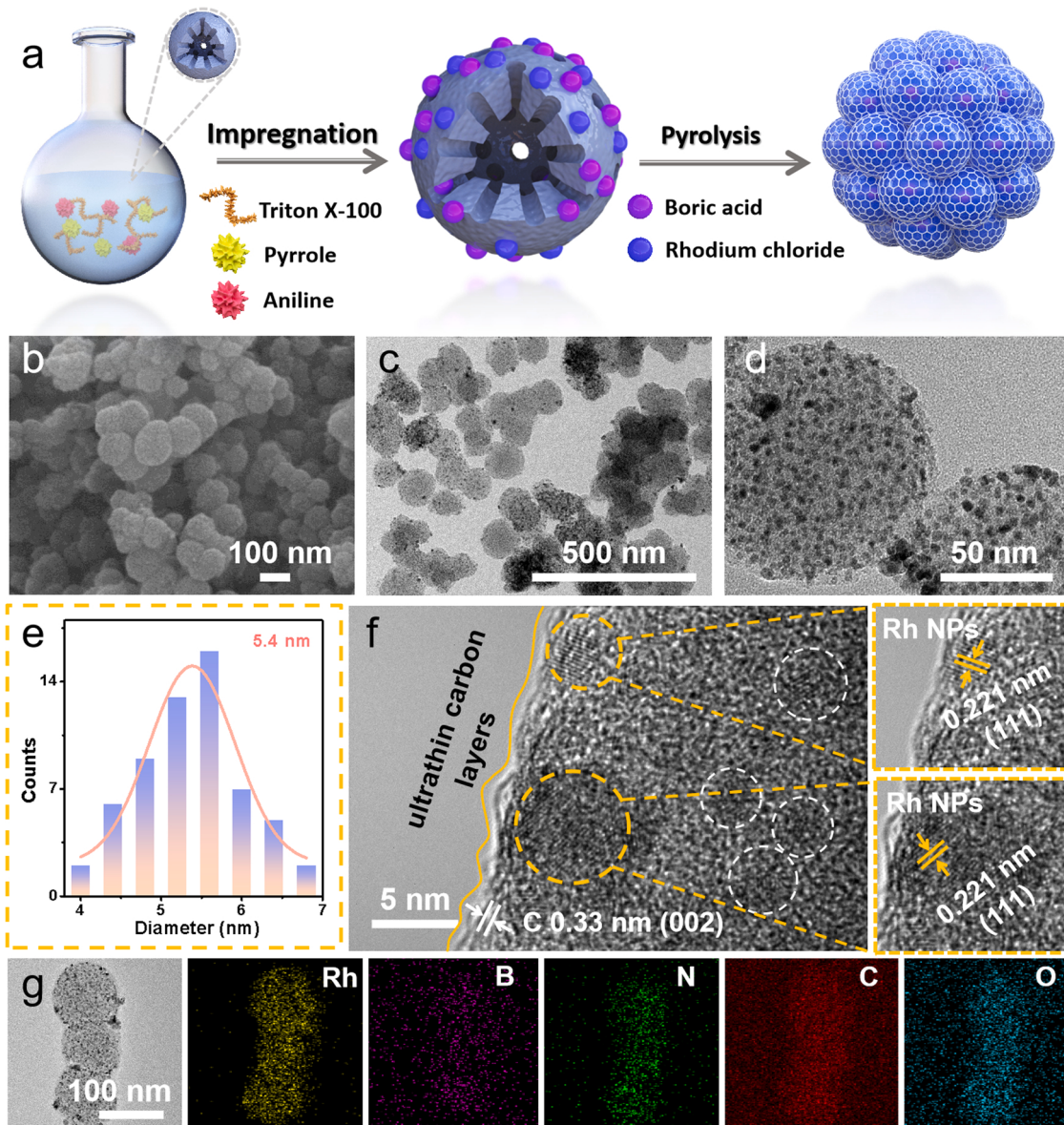


Fig. 1. (a) Schematic illustration of the preparation process for the B-Rh@NC nanospheres. (b) SEM image, (c, d) TEM images of B-Rh@NC. (e) The size distribution of nanoparticles. (f) HRTEM image, and (g) TEM image and Rh, B, N, C, and O element mapping images of B-Rh@NC.

samples were obtained under the same condition except that the mole ratio of $\text{RhCl}_3 \cdot 3 \text{ H}_2\text{O}$ and H_3BO_3 was set to 1:2 and 1:6 as opposed to 1:4.

2.3. Synthesis of NC, B-NC, and Rh@NC nanospheres control samples

NC, B-NC, and Rh@NC nanospheres were prepared using the similar method as B-Rh@NC, except that $\text{RhCl}_3 \cdot 3 \text{ H}_2\text{O}$ and H_3BO_3 were not added for NC, $\text{RhCl}_3 \cdot 3 \text{ H}_2\text{O}$ was not added for B-NC, and H_3BO_3 was not added for Rh@NC.

Specific related test methods are provided in the [Supporting Information](#).

3. Results and discussion

3.1. Preparation and characterization of B-Rh@NC nanospheres

The synthesis process for B-Rh@NC nanospheres with ultrafine Rh NPs encapsulated by ultrathin B and N co-doped carbon layers is displayed in [Fig. 1a](#). Typically, polyaniline-pyrrole nanospheres obtained with the assistance of Triton X-100 surfactant serve as C source and structure directing agent. At the same time, Rh and B are introduced into the carbon matrix by the pyrolysis of RhCl_3 and H_3BO_3 at the high temperature. Briefly, polymer nanospheres are mixed with RhCl_3 and

H_3BO_3 and heated at 800 °C in inert gas. Under the action of high temperatures, boron doping activates the SMSI between ultra-small Rh NPs and N-doped graphitic carbon matrix. Representative morphology and structure of the B-Rh@NC catalyst was firstly characterized by SEM and TEM images. As revealed by SEM images ([Figs. 1b and S1](#)), the morphology of B-Rh@NC are well-defined nanospheres which have narrow diameter distributions with the average diameter of ~100 nm. TEM image of the B-Rh@NC shows well-dispersed pitaya-like structure without obvious aggregation and numerous NPs are homogeneously embedded into the internal holes on carbon surface ([Figs. 1c and d](#)). The suitable pyrolysis of carbon nanospheres as support can prohibit Rh NPs from growing larger. Meanwhile, numerous NPs centered in the size of 3–8 nm are observed on each carbon nanosphere ([Fig. 1e](#)). Further HRTEM analysis confirms that metal NPs are completely encapsulated by rather thin 1–3 carbon layers. Form the enlarged picture of HRTEM image, 0.221 nm lattice fringes are clearly observed, which is indexing to the (111) plane of Rh phase ([Fig. 1f](#)). To further explain the formation process of the B-Rh@NC nanospheres, TEM images of NC, B-NC ([Fig. S2](#)), and Rh@NC ([Fig. S3](#)) compounds were further investigated. As is revealed from these TEM images, NC, B-NC, and Rh@NC exhibit the same spherical morphology with the similar size to that of B-Rh@NC, which verify that the addition of Rh and B into polymer structure do not change the morphology of carbon framework during high-temperature

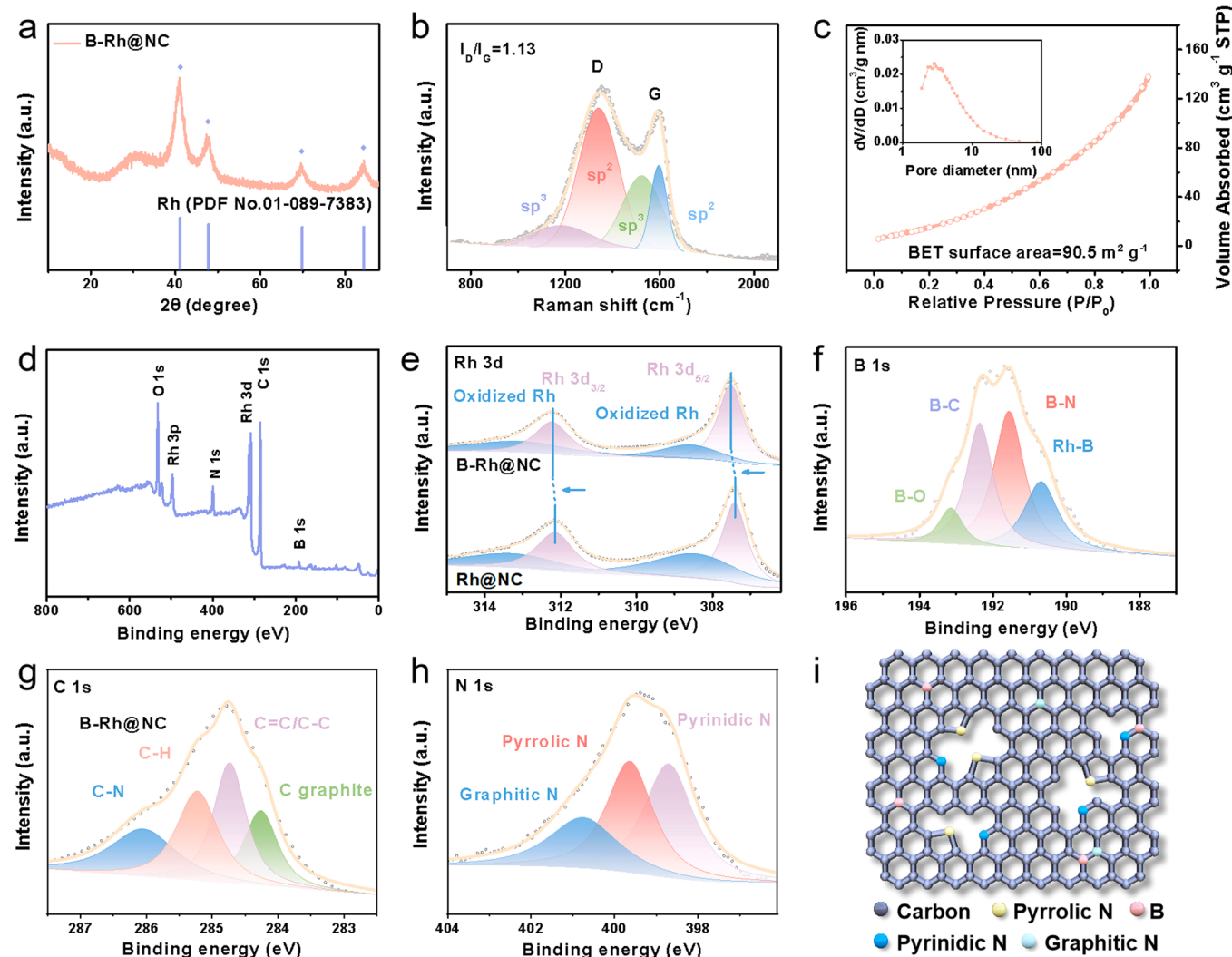


Fig. 2. (a) XRD pattern, (b) Raman spectrum, (c) N_2 adsorption-desorption isotherm (Inset: pore size distribution) of B-Rh@NC. (d) Survey XPS spectrum of B-Rh@NC. (e) High-resolution XPS scans of B-Rh@NC and Rh@NC at Rh 3d. (f-h) High-resolution XPS scans of B-Rh@NC at (f) B 1s, (g) C 1s, and (h) N 1s. (i) Schematic illustration of the N and B doped carbon present in B-Rh@NC.

pyrolysis process, indicating the stable property of polymer nanospheres. In addition, the lattice fringes of 0.220 nm in the HRTEM image can be indexed to the (111) plane of Rh for Rh@NC. The essence of the doping in the B-Rh@NC is disclosed by the TEM elemental mappings and EDX of Rh, B, N, C, and O (Figs. 1g and S4). As expected, Rh, B, N, C, and O atoms are distributed homogeneously over every carbon nanosphere without obvious aggregation. Furthermore, the ICP-AES measurement is employed to get the precise element content, and the Rh element accounts for the weight percentage of 8.3%, which is much less than that of the commercial 20% Pt/C.

The XRD pattern of B-Rh@NC further confirmed that the metal NPs encapsulated by rather thin carbon layers were composed of Rh NPs. As shown in Fig. 2a, the XRD pattern shows the distinct (111), (200), (220), (311), and (222) diffraction peaks of Rh without other impurities, thus indicating the formation of cubic phase of Rh (PDF No. 01-089-7383). For comparison, XRD patterns of Rh@NC and B-NC are also displayed in Figs. S5a and b. The XRD pattern of Rh@NC is consistent with that of B-Rh@NC, which is also composed of cubic Rh phase, indicating the high purity of both B-Rh@NC and Rh@NC. Additionally, the typical peak for all these catalysts observed at $\sim 23.5^\circ$ are indexed to the (002) plane of graphitic carbon, indicating the partial graphitization of carbon substrates. Raman spectra was further used to study the graphitization degree of the B-Rh@NC composite because the D (1345 cm^{-1}) and G (1590 cm^{-1}) bands provide the disorder and crystallinity of sp^2 carbon materials, respectively [28]. As shown in Fig. 2b, the value of I_D/I_G is calculated to be 1.13, consistent with the XRD result, also implying the partial graphitization of carbon matrix, which is in favor of improving the electrical conductivity of catalyst [29–31]. In addition, the N_2 adsorption-desorption isotherms of B-Rh@NC measured at 77 K was shown in Fig. 2c. The specific surface area based on BET method is measured as high as $90.5\text{ m}^2\text{ g}^{-1}$. The inset in Fig. 2c describes the pore size distribution based on the BJH method, implying that major pores center on the mesoporous size, and the formation of mesopores mainly derive from the

pyrolysis of Rh/B-blended nanospheres. Such porous B-Rh@NC structure with large surface area enables full exposing of rich active metallic species and increasing the contact area between electrode and electrolyte during electrocatalysis process. To make a deep understanding to the detailed elemental compositions and surface chemical states, X-ray photoelectron spectroscopy (XPS) of all catalysts were performed. The full survey XPS spectrum of B-Rh@NC (Fig. 2d) indicates the presence of Rh, B, C, N, and O elements, consistent with the above TEM mapping results (Fig. 1g). The Rh 3d spectrum are divided into four main peaks. The component at 307.5 and 312.2 eV is assigned to $3d_{5/2}$ and $3d_{3/2}$ of Rh, while the one at 308.6 and 313.4 eV is attributed to Rh oxides (Fig. 2e) [32–34]. By comparing with the Rh 3d spectrum of B-Rh@NC and Rh@NC, it can be found that the Rh 3d binding energy of B-Rh@NC shifts negatively compared to that of Rh@NC (Fig. 2e). This is because that the vacant $2p_z$ orbital of B can conjugate with the π electrons of carbon substrate, while these electrons are quite active because of the low electronegativity of B, thus leading to the rich electron density around Rh atoms. The B 1 s XPS spectrum (Fig. 2f) can be deconvoluted into four peaks of B-O (193.2 eV), B-C (192.4 eV), B-N (191.6 eV), Ru-B (190.7 eV), respectively [35]. This result demonstrates that B atoms are doped into carbon matrix. It should be noted that the binding energy of Ru-B shifts positively by comparing with the binding energy of pure boron (~ 187 eV), indicating partial electron transfer from B to Ru, making Ru bear rich electrons and B bear deficient electrons. The existence of B-O bond (193.2 eV) is associated with the surface oxidation. The spectrum of C 1 s in B-Rh@NC (Fig. 2g) possesses four peaks at 284.2, 284.6, 285.2, and 286 eV, which can be assigned to C graphite, C=C/C-C, C-H, and C-N, respectively. Three N types of N species, including pyridinic N (398.7 eV, 47%), pyrrolic N (399.8 eV, 35.6%), and graphitic N (401.2 eV, 17.4%), can be observed from the N 1 s spectrum (Fig. 2h) [36]. Fig. 2i displays the clear molecule model of N and B heteroatoms in carbon matrix. It should be noted

that the existence of B atom and different coordinations of N with distinct electronic environments near neighboring C atoms in the B-Rh@NC catalyst may improve the electrocatalytic activity by interacting with OH^- or H^+ for the HER. As comparison, the detailed elemental compositions and surface chemical states of Rh@NC and B-NC are also presented in Figs. S6 and S7, further validating the synthesis of these two compounds.

To further interpret the inner relations of the structure and the HER performance of the B-Rh@NC nanospheres, a series of control samples by varying the mole ratio of B/Rh were prepared under the same pyrolysis temperature. The SEM images of B-Rh@NC series samples confirm their similar pitaya-like structure, of which numerous NPs are homogeneously distributed on every nanosphere (Fig. S8), indicating the high thermal stability of the polyaniline-pyrrole nanospheres as carbon framework. However, it can be clearly observed that the inner NPs embedded in carbon shells gradually aggregate with the increasing of B species. To further explore the composition of inner NPs, TEM images of B-Rh@NC series samples are presented. It can be seen from Fig. S9 that the B phase appears with the increased B amount, so an optimized B/Rh ratio is demanded to realize the high purity of Rh phase. The same result is also reflected from XRD patterns of B-Rh@NC series samples in Fig. S10a. As observed, B-Rh@NC with excessive B amount (Rh/B ratio of 1:6) are composed of Rh and B hybrids, but only the typical peaks of Rh phase can be observed in B-Rh@NC (1:2) and B-Rh@NC (1:4). Interestingly, the values of I_D/I_G reflected from Raman spectra gradually decrease from 1.19 to 1.12 when the with the increase of B species (Fig. S10b). This result indicates that the addition of B species is beneficial for forming more ordered graphitic carbon. In addition, the BET surface area of B-Rh@NC series samples with the Rh/B ratio of 1:2 is the highest (Fig. S10c), illustrating that appropriate amount of B doping promotes the formation of porous B-NC shells.

3.2. Electrocatalytic performance of B-Rh@NC for HER

The electrocatalytic activity of B-Rh@NC was firstly investigated in 0.5 M H_2SO_4 media and Bare GCE, commercial Pt catalyst (20 wt% Pt/C), NC, B-NC, Rh@NC have also been investigated as reference. As displayed in Fig. 3a, Bare GCE and NC shows negligible poor HER activities, while the B-Rh@NC shows an onset potential of about 0 V which is close to the Pt/C and thermodynamic potential of HER. The B-Rh@NC shows a small overpotential (43 mV) to reach a current density of 10 mA cm^{-2} , which is much lower than of undoped Rh@NC (110 mV), and only slightly larger than that of Pt/C catalyst (25 mV). Importantly, the HER activity of B-Rh@NC exceeds commercial Pt/C when the current density reaches 60 mA cm^{-2} . This result suggests that B-doped into carbon shells can effectively improve the HER activity of B-Rh@NC, and the small overpotential indicates that B-Rh@NC is among the most active HER electrocatalyst for HER in harsh acidic medium (Table S1). Furthermore, the mass activities of B-Rh@NC and commercial Pt/C were calculated, and the mass activities of B-Rh@NC is much higher than Pt/C at full overpotential range (Fig. 3b). To investigate the intrinsic kinetics for HER process, tafel plots of as-prepared catalysts fitted from the

polarization curves were carried out. Usually, HER process in acid involves three major reactions, including the first step of discharge reaction (Volmer reaction, 120 mV dec^{-1}), and followed by ion^+ atom reaction (Heyrovsky reaction, 40 mV dec^{-1}) or combination reaction (Tafel reaction, 30 mV dec^{-1}) [37]. As displayed in Fig. 3c, B-Rh@NC yields a Tafel slope of 52 mV dec^{-1} , much lower than Rh@NC (97 mV dec^{-1}) and B-NC (226 mV dec^{-1}) control samples, and slightly higher than that of Pt/C (27 mV dec^{-1}), indicating the favorable reaction kinetics for HER. The Tafel slope of 52 mV dec^{-1} for B-Rh@NC demonstrates the typical Volmer-Heyrovsky mechanism, in which the ion^+ atom reaction is the rate determining step. As shown in Fig. 3d that B-Rh@NC has a high exchange current density (1.52 mA cm^{-2}), which indicating B-Rh@NC requires a small driving force to carry out HER reaction. Electrochemical impedance spectra (EIS) measurement was

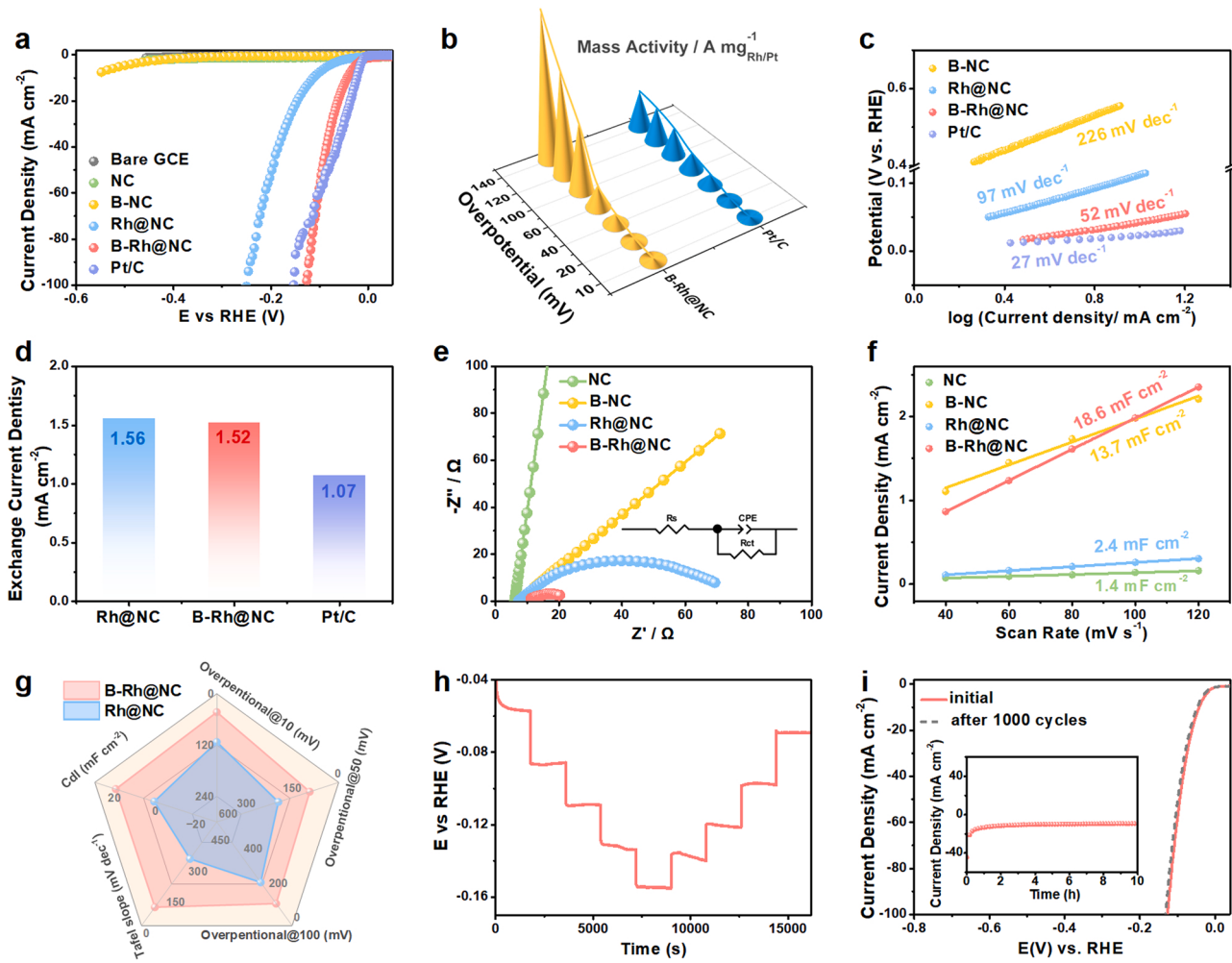


Fig. 3. (a) LSV curves of various catalysts at a scan rate of 5 mV/s in 0.5 M H_2SO_4 . (b) Mass activity of B-Rh@NC and Pt/C. (c) Tafel plots. (d) Comparison of exchange current density. (e) Nyquist plots of various catalysts. (f) Double-layer capacitances of various catalysts. (g) Comprehensive comparisons of the HER performance of B-Rh@NC with Rh@NC. (h) multi-step chronopotentiometry of B-Rh@NC. (i) LSV curves of B-Rh@NC before and after 1000 CV cycles (Inset: i-t curves tested at 50 mV for 10 h).

also carried to investigate the reaction kinetics of B-Rh@NC. The Nyquist plots were measured to assess the reaction kinetics of catalysts. Compared with Rh@NC (61.5Ω) and B-NC (291Ω), B-Rh@NC displays a much lower R_{ct} value of 9.5Ω , indicating the faster reaction kinetics (Fig. 3e). The favorable charge transport ability of B-Rh@NC mainly originates from the SMSI interaction between the partial graphitization ($I_D/I_G=1.13$) and Rh NPs in the nanospheres, thus higher HER catalytic activity is realized (Fig. 2b). To figure out the different performances of various catalysts, electrochemically surface areas (ECSA) were estimated from the double-layer capacitance (C_{dl}) (Fig. S11). As displayed in Fig. 3f, the measured C_{dl} values of NC, B-NC, Rh@NC, and B-Rh@NC are evaluated to be 1.4, 13.7, 2.4, and 18.6 mF cm^{-2} , respectively. The C_{dl} value of B-Rh@NC is larger than other electrodes, indicating a large ECSA towards HER with abundant active sites. It can be concluded that B-doped into carbon matrix can produce more defects of carbon shells, thus enabling the full exposure of active species. B-Rh@NC has the excellent HER activity as compared to undoped Rh@NC (Fig. 3g). Durability is an important factor to evaluate the performance of electrocatalyst. Fig. 3h illustrated the multi-step chronopotentiometry of B-Rh@NC from the current densities of 20 mA cm^{-2} to 100 mA cm^{-2} with the identical intervals. It can be clearly observed that the potential has no obvious decay after long time continuous test, demonstrating the excellent mass transport property and durability of B-Rh@NC. In addition, the durability of the B-Rh@NC in acidic media was performed

using long-term potential cycling at an accelerated scanning rate of 100 mV s^{-1} . The LSV curve of B-Rh@NC shows negligible current density loss after 1000 cycles in acid, demonstrating the excellent durability (Fig. 3i). Moreover, the practical operation of the B-Rh@NC was also measured by electrolysis at static potentials of 50 mV for 10 h. As shown in set of Fig. 3i, the stable current density over 10 h with slight loss are presented, which further suggests the excellent stability of B-Rh@NC hybrid for HER. The SEM and TEM mapping images were further observed to explore the structure changes of B-Rh@NC catalyst after long time stability test. It can be seen from Fig. S12 that there exhibits no obvious aggregation of nanospheres after stability test, which clearly confirms the stable structure of carbon framework of the B-Rh@NC. Besides, as shown in Fig. S13, TEM and TEM mappings of B-Rh@NC after reaction suggest that inner Rh nanoparticles with homogeneous distribution are still well embedded in the carbon shells after reaction, further confirming the high durability of B-Rh@NC. The above electrocatalytic results clearly reveal the excellent activity of B-Rh@NC and the carbon layers coating on the outer layer of the B-Rh@NC. And the excellent stability is derived from the carbon layers coating on the outer layer of the B-Rh@NC, which can effectively avoid the corrosion of the catalyst under harsh acidic medium.

Encouraged by the Pt-like activity for HER in acidic solution, the catalytic activities of B-Rh@NC electrode for HER in alkaline and neutral media were also investigated. As expected, the B-Rh@NC also

displays excellent HER performance in 1.0 M KOH and 1.0 M PBS. As shown in Fig. 4a, B-Rh@NC needs a much low overpotential of only 26 mV to drive a current density of 10 mA cm^{-2} , which is even superior to that of Pt/C and other samples (Fig. 4b). The corresponding Tafel slope of B-Rh@NC is 49 mV dec^{-1} , which is smaller than those of B-NC (145 mV dec^{-1}), Rh@NC (59 mV dec^{-1}), and Pt/C (50 mV dec^{-1}) (Fig. S14a), and most of the recently reported noble metal-based electrocatalysts (Fig. 4a, g and Table S2). In addition, B-Rh@NC displays a low impedance with the R_{ct} of 27Ω , a large C_{dl} of 14.4 mF cm^{-2} calculated from CV curves (Fig. S14b-d). The successive CV cycling measurement and chronoamperometry i-t curve both demonstrate excellent long-term stability of B-Rh@NC in 1.0 M KOH (Fig. 4c). Moreover, the SEM image, TEM image, and TEM mappings of B-Rh@NC reveal that the spherical structure of the B-Rh@NC are well maintained and the Rh, B, C, N, and O elements are well-dispersed throughout every nanosphere without obvious aggregation after long-term stability tests, in consistent with the stable property of the B-Rh@NC in wide pH range (Figs. S15 and S16). Interestingly, B-Rh@NC also exhibit excellent performance in neutral media, as is reflected from the low overpotential of 70 mV to drive 10 mA cm^{-2} , small Tafel slope of 56 mV dec^{-1} , a low R_{ct} of 40.8Ω , and a large C_{dl} of 19.7 mF cm^{-2} , which is superior to those

of NC, B-NC, Rh@NC, even Pt/C when the current density exceeds 40 mA cm^{-2} (Fig. 4d, e and S17), and most of reported noble metal-based catalysts (Fig. 4g and Table S3). Stability tests performed by CV and chronoamperometry i-t measurement, SEM, TEM, TEM mappings after stability test all prove the high durability and stable structure of B-Rh@NC in neutral solution (Figs. 4f, S18, and S19). Overall, these results clearly confirm that the B-Rh@NC nanospheres displays highly active and stable HER performance under various pH value (Fig. 4h).

In control experiments, the effect of the B content on HER performance were also investigated. The HER activities of B-Rh@NC with the different Rh/B ratio are evaluated. As displayed in Fig. S20, B-Rh@NC with the Rh/B ratio of 1:4 shows the lowest overpotential of 42 mV to drive 10 mA cm^{-2} , the smallest Tafel slope of 52 mV dec^{-1} , the lowest R_{ct} of 9.5Ω , and the C_{dl} values of 18.6 mF cm^{-2} among three samples in 0.5 M H_2SO_4 . In accordance with the results observed in acidic media, B-Rh@NC obtained with the Rh/B ratio of 1:4 also displays the superior HER activity to the B-Rh@NC with the Rh/B ratio of 1:2 and 1:6 both in alkaline and neutral media (Figs. S19 and S20). The B-Rh@NC with the Rh/B ratio of 1:4 exhibits the optimal HER activity in a pH-universal solution, possibly because it integrates the merits of the purity of Rh phase, well-dispersed active species, and the optimal graphitization.

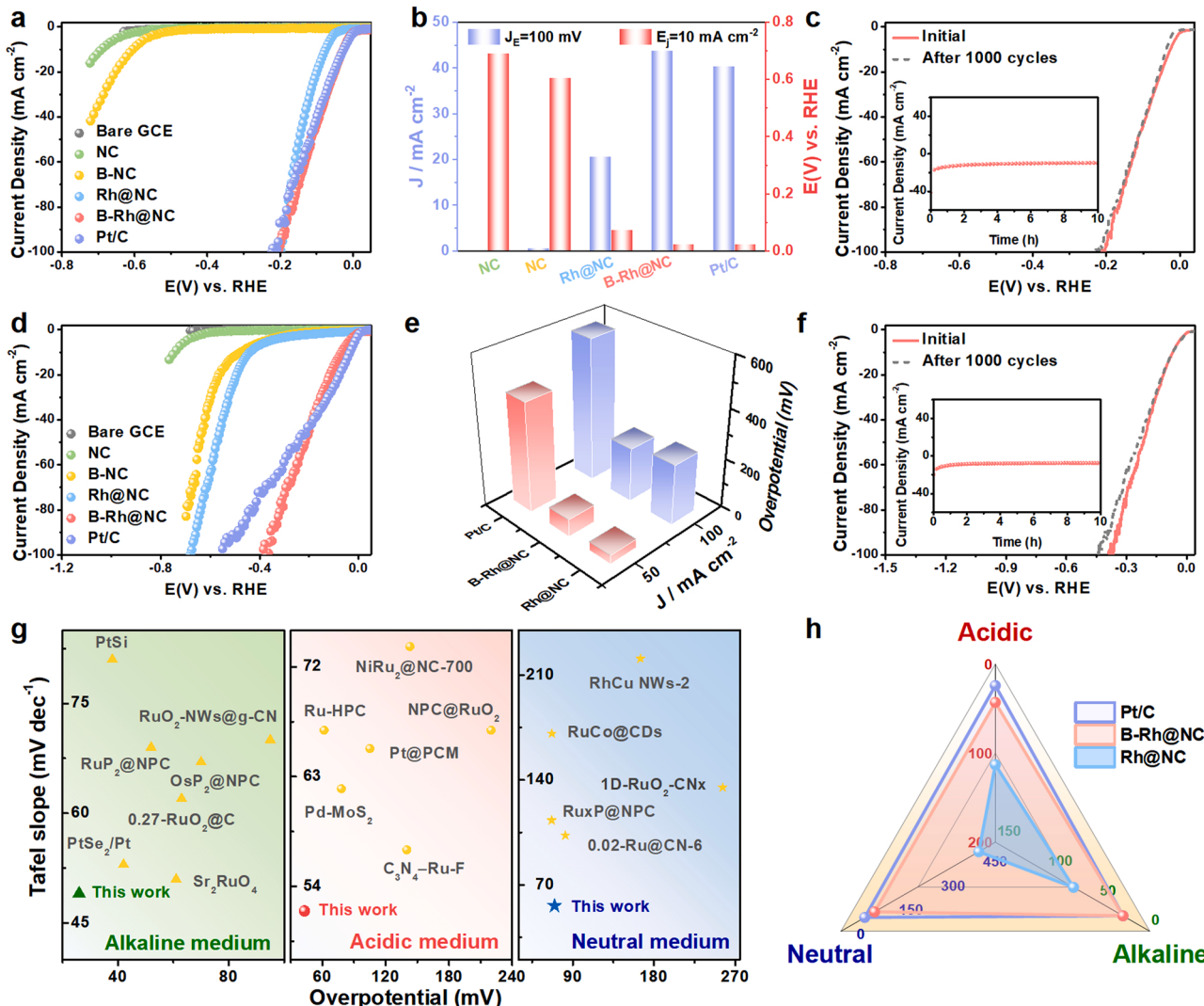


Fig. 4. (a, d) LSV curves of various catalysts at a scan rate of 5 mV s^{-1} in (a) 1.0 M KOH and (d) 1.0 M PBS. (b, e) Overpotentials and current densities of B-Rh@NC in (b) 1.0 M KOH and (e) 1.0 M PBS. (c, f) LSV curves of B-Rh@NC before and after 1000 CV cycles (Inset: i-t curves tested at 50 mV in (c) 1.0 M KOH and 100 mV in (f) 1.0 M PBS for 10 h, respectively). Comprehensive comparisons of the HER performance of B-Rh@NC with (g) reported catalysts in literature and (h) as-prepared samples in full pH range.

Overall, the above electrochemical results demonstrate that the ratio of Rh/B has great influence on the HER performance.

3.3. Investigation on the OWS performance in a two-electrode system

Considering the outstanding HER catalytic performance, we further investigated the overall water splitting performance by integrating B-Rh@NC and RuO₂ into a two-electrode alkaline electrolyzer. The polarization curve (Fig. 5a) shows the excellent activity of the B-Rh@NC || RuO₂ electrolyzer for overall water splitting with low cell voltages of 2.12 and 2.29 V to drive high current densities of 1 and 3 A cm⁻², which is superior to that of Pt/C || RuO₂ electrolyzer and other reported catalysts (Fig. 5b and Table S4). Furthermore, the multi-step chronopotentiometry curve (Fig. 5c) shows negligible degradation after continuous operation, indicating the remarkable stability of B-Rh@NC || RuO₂ for overall water splitting. The amount of H₂/O₂ were collected by the water drainage method in the H-type electrolytic cell (Fig. 5d and e). The faradaic efficiency of B-Rh@NC is demonstrated to be close to 100% for H₂, approaching the theoretical value during electrolysis (Fig. 5f). For the practical application, the electrolyzer can be driven by a commercial solar panel. As shown in Fig. 5h, H₂ and O₂ bubbles are obviously observed on the surface of B-Rh@NC and RuO₂, respectively. Meanwhile, the electrolyzer can be powered by the Stirling engine. Numerous apparent bubbles took shape on the electrodes during the electrocatalytic process (Fig. 5g). These results manifest that B-Rh@NC

owned efficient and durable performance toward water splitting.

3.4. Theoretical investigation

In order to reveal the possible mechanism of the Pt-like performance after B-doping for B-Rh@NC, the DFT calculations are employed for HER process. Combined with the above experimental results, we construct the correlative theoretical models including B-Rh@NC and Rh@NC as shown in Figs. 6a and S23. Besides, the corresponding Bader charge distribution of B-Rh@NC (Fig. 6b) and Rh@NC (Fig. S24) were further calculated. Compared with Rh@NC, the Rh unit cells in B-Rh@NC lose more charge, so it can be considered that the B doped can make B-Rh@NC gain electrons easily, thereby promoting the reaction kinetics. The charge redistribution is dominantly restricted on B doped Rh and B doped NC. Specifically, the charge is accumulated in the region of B doped NC while depleted around the Rh and neighboring B (Fig. 6c) [38, 39]. These results demonstrate that B doping may activate the SMSI further facilitating the absorption of H₂O, which can boost the HER catalytic activity. To explore the local distribution characteristics of electrons, the electronic local function (ELF) of B-Rh@NC (Fig. 6d) and Rh@NC (Fig. S25) was analyzed, respectively. The ELF of B-Rh@NC suggests that electrons at the interface of B-Rh cluster and B-NC were strongly delocalized, thus accelerating the electron

transfer from B-NC to B-Rh under the external electric potential. In order to unravel the active site in the B-Rh@NC was investigated by

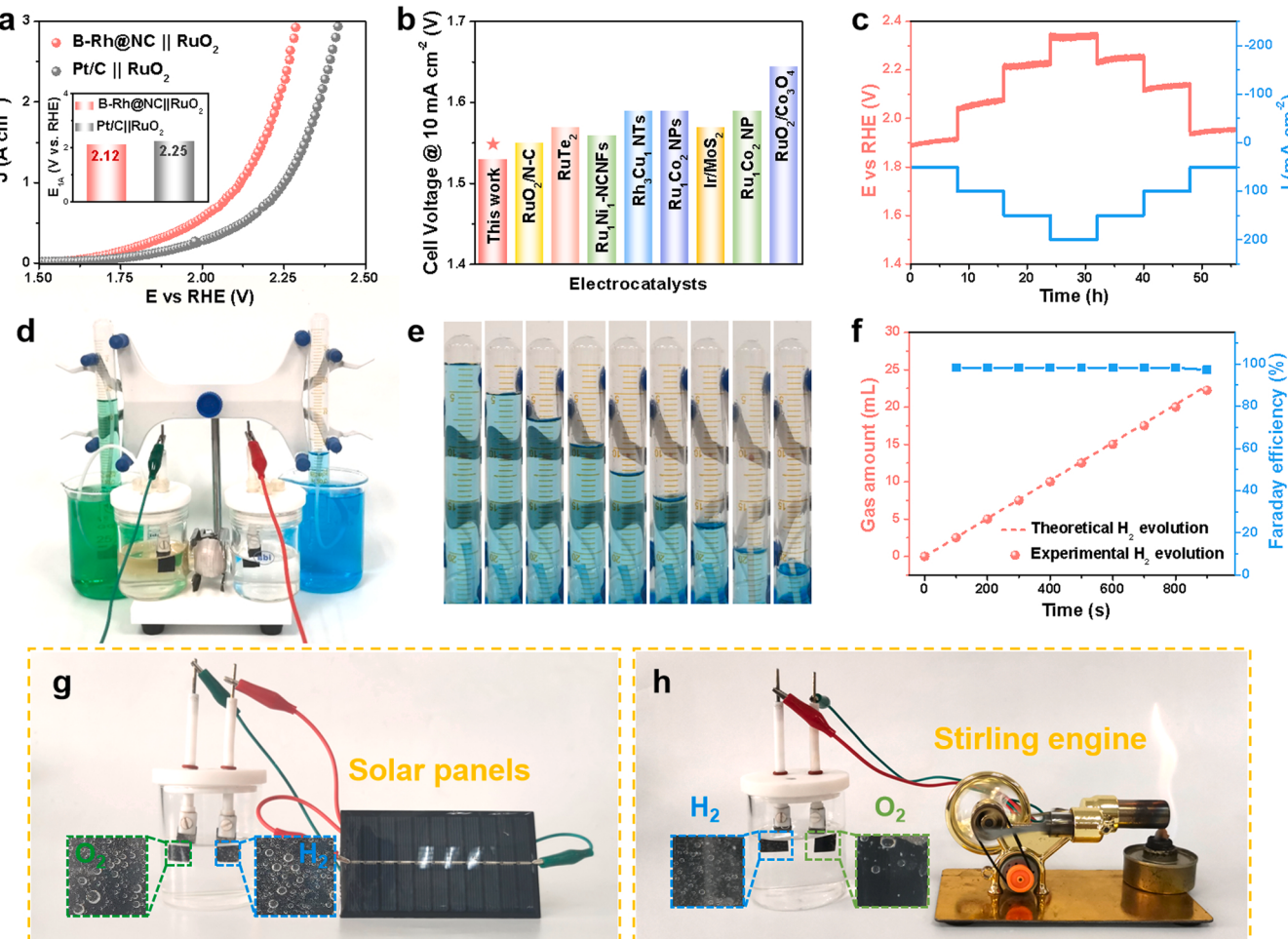


Fig. 5. (a) LSV curves of B-Rh@NC for water splitting in 1.0 M KOH solution. (b) Performance comparison for recently reported electrocatalysts. (c) Multistep chronopotentiometry of B-Rh@NC. (d) Faradaic efficiency measurement device based on water splitting. (e) Photographs of H₂ collected at different times. (f) The amount of H₂ and faraday efficiency varying with time. (g) Optical image of B-Rh@NC || RuO₂ electrode pairs driven by solar cell. (h) Photograph of water splitting process powered by a Stirling engine operating 1.0 M KOH solution.

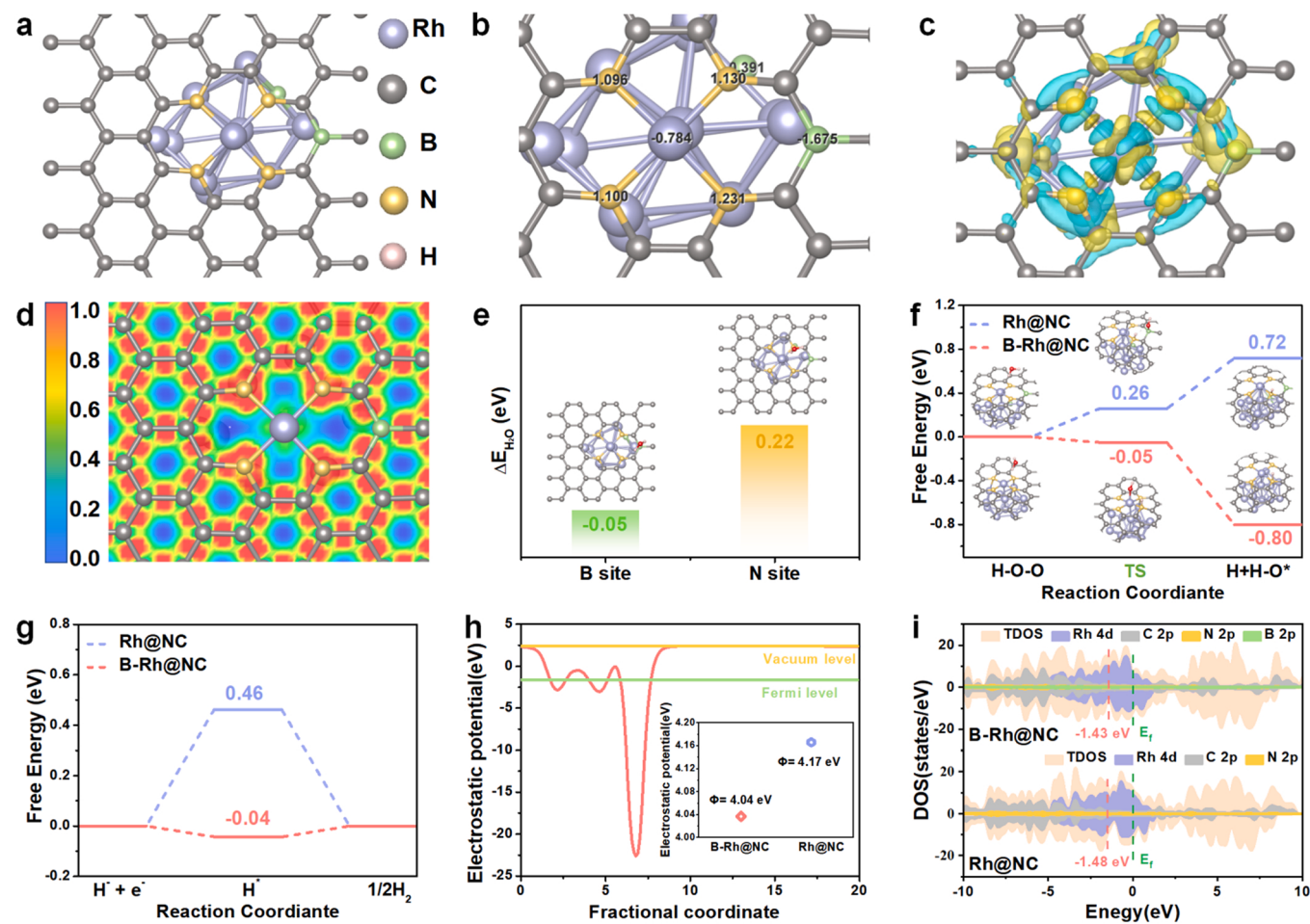


Fig. 6. (a) The atomic structure models of B-Rh@NC. (b) The Bader charge analysis; (c) The charge density difference analysis for B-Rh@CN with the cyan region representing charge depletion and the yellow region representing charge accumulation. (d) ELF of B-Rh@CN. (e) Water adsorption energy on B-Rh@CN and Rh@CN, the inset are the most stable configurations of the H_2O adsorbed intermediate. (f) Transition barrier for H_2O dissociation on surface of B-Rh@CN and Rh@CN. (g) Free energy profiles of HER for B-Rh@CN and Rh@CN. (h) The computed work functions of B-Rh@CN. (i) The density of states of B-Rh@NC and Rh@NC.

comparing the adsorption ability of H_2O molecular on B and N sites on the surface of B-Rh@NC, respectively. As shown in Fig. 6e, the water adsorption energy ($\Delta E_{\text{H}_2\text{O}}$) of B site (-0.05 eV) and N site (0.22 eV) on the B-Rh@NC surface are investigated. The adsorption of H_2O molecule is energetically more favorable on the B site of B-Rh@NC surface, implying that B atoms are the active sites in the HER process. [40]. The low kinetic energy barrier of the water dissociation on the catalyst surface are responsible for the fast HER kinetics in alkaline solution, the calculated water dissociation energy on these surfaces was presented in Fig. 6f. As expected, the B-Rh@NC possesses a lower energy barrier of transition state (-0.05 eV) than that of Rh@NC (0.26 eV), indicating that B-Rh@NC has fast reaction kinetics for water dissociation and thus guarantees effective water dissociation. The free energy of hydrogen absorption (ΔG_{H^*}) was calculated to explore possible origins of high HER activity. Compared with Rh@NC (0.46 eV), the ΔG_{H^*} of B-Rh@NC (-0.04 eV) is closer to the thermoneutral value (Fig. 6g) [41]. The above results show that the strong SMSI between the N-doped carbon matrix and ultra-small Rh NPs synergistically facilitating hydrogen adsorption/desorption behavior, which is consistent with outstanding HER activity of B-Rh@NC. To further study the electronic migration, the work function was conducted (Figs. 6h and S26). The lowest work function of B-Rh@NC (4.04 eV) implies its highest surface electron activity. The density of states (DOS) for Rh@NC and B-Rh@NC were calculated as presented in Fig. 6i. Compared to Rh@NC (-1.48 eV), the d-band center of B-Rh@NC (-1.43 eV) notably shifts to Fermi level (E_f) after B doping, which clearly demonstrates that hydrogen adsorption is

promoted [42].

4. Conclusion

In summary, we have presented a novel boron doping strategy to activate the SMSI of ultra-small Rh@NC nanoparticles. Experimental and theoretical studies prove that the boron doping optimize the electronic structure and the water adsorption energy, and further activate the SMSI of Rh and NC. As a result, the obtained B-Rh@NC displays outstanding electrocatalytic activity for HER in a wide pH range and with excellent durability. Additionally, with B-Rh@NC and RuO₂ as cathode and anode, respectively, the assembled two electrode system only need 1.53 V to drive 10 mA cm^{-2} in 1.0 M KOH . The current work paves a new avenue to design Rh-based electrocatalyst with high efficiency for HER in full pH range.

CRediT authorship contribution statement

Qingping Yu: Investigation, Data curation, Conceptualization, Formal analysis, Validation, Writing – original draft. **Yixin Fu:** Validation. **Jiarui Zhao:** Validation. **Bin Li:** Validation. **Xinping Wang:** Validation. **Xiaobin Liu:** Conceptualization, Writing – review & editing, Supervision, Funding acquisition. **Lei Wang:** Writing – review & editing, Funding acquisition, Supervision.

Declaration of Competing Interest

The authors declare that they have no known competing financial interests or personal relationships that could have appeared to influence the work reported in this paper.

Data availability

The authors do not have permission to share data.

Acknowledgments

Financial support from the National Natural Science Foundation of China (51772162, 21971132 and 52072197), China Postdoctoral Science Foundation (2020M682135), Postdoctoral Applied Research Project of Qingdao, Outstanding Youth Foundation of Shandong Province, China (ZR2019JQ14), Postdoctoral Innovation Project of Shandong Province (202102039), Youth Innovation and Technology Foundation of Shandong Higher Education Institutions, China (2019KJC004), Major Scientific and Technological Innovation Project (2019JZZY020405), Major Basic Research Program of Natural Science Foundation of Shandong Province under Grant (ZR2020ZD09), Taishan Scholar Young Talent Program (tsqn201909114), and Talent Foundation funded by Province and Ministry Co-construction Collaborative Innovation Center of Eco-chemical Engineering (STHGYX2202).

Appendix A. Supplementary material

Supplementary data associated with this article can be found in the online version at [doi:10.1016/j.apcatb.2022.122297](https://doi.org/10.1016/j.apcatb.2022.122297).

References

- Y. Luo, L. Tang, U. Khan, Q. Yu, H. Cheng, X. Zou, B. Liu, Morphology and surface chemistry engineering toward pH-universal catalysts for hydrogen evolution at high current density, *Nat. Commun.* 10 (2019) 1903137–1903150, <https://doi.org/10.1038/s41467-018-07792-9>.
- H. Zhang, J. Wang, F. Qin, H. Liu, C. Wang, V-doped Ni₃N/Ni heterostructure with engineered interfaces as a bifunctional hydrogen electrocatalyst in alkaline solution: simultaneously improving water dissociation and hydrogen adsorption, *Nano Res.* 14 (2021) 3489–3496, <https://doi.org/10.1007/s12274-021-3559-9>.
- Q. Zhang, H. Bai, Q. Zhang, Q. Ma, Y. Li, C. Wan, G. Xi, MoS₂ yolk-shell microspheres with a hierarchical porous structure for efficient hydrogen evolution, *Nano Res.* 9 (2016) 3038–3047, <https://doi.org/10.1007/s12274-016-1186-7>.
- M. Ge, X. Zhang, S. Xia, W. Luo, Y. Jin, Q. Chen, H. Nie, Z. Yang, Uniform formation of amorphous cobalt phosphate on carbon nanotubes for hydrogen evolution reaction, *Chin. J. Chem.* 39 (2021) 2113–2118, <https://doi.org/10.1002/cjoc.202000695>.
- Y. Wang, G. Qian, Q. Xu, H. Zhang, F. Shen, L. Luo, S. Yin, Industrially promising IrNi-FeNi₃ hybrid nanosheets for overall water splitting catalysis at large current density, *Appl. Catal. B Environ.* 286 (2021) 119881–119887, <https://doi.org/10.1016/j.apcatb.2021.119881>.
- J. Wang, B. Guo, J. Sun, Y. Zhou, C. Zhao, Z. Wei, J. Guo, Cooperative hydrogen evolution reaction combining Cu₂₊O and Ru active sites, *Appl. Catal. B Environ.* (2022), 122169, <https://doi.org/10.1016/j.apcatb.2022.122169>.
- K. Zhang, Y. Duan, N. Graham, W. Yu, Unveiling the synergy of polymorph heterointerface and sulfur vacancy in NiS/Ni₃S₂ electrocatalyst to promote alkaline hydrogen evolution reaction, *Appl. Catal. B Environ.* 323 (2023), 122144, <https://doi.org/10.1016/j.apcatb.2022.122144>.
- Y. Guo, B. Hou, X. Cui, X. Liu, X. Tong, N. Yang, Pt atomic layers boosted hydrogen evolution reaction in nonacidic media, *Adv. Energy Mater.* (2022) 2201548–2201558, <https://doi.org/10.1002/aenm.202201548>.
- S. Anantharaj, V. Aravindan, Developments and perspectives in 3d transition-metal-based electrocatalysts for neutral and near-neutral water electrolysis, *Adv. Energy Mater.* 10 (2019) 1902666–1902695, <https://doi.org/10.1002/aenm.201902666>.
- X. Fu, J. Zhang, S. Zhan, F. Xia, C. Wang, D. Ma, Q. Yue, J. Wu, Y. Kang, High-Entropy alloy nanosheets for fine-tuning hydrogen evolution, *ACS Catal.* (2022) 11955–11959, <https://doi.org/10.1021/acscatal.2c02778>.
- C. Sun, P. Zhao, Y. Yang, Z. Li, W. Sheng, Lattice oxygen-induced d-band shifting for enhanced hydrogen oxidation reaction on nickel, *ACS Catal.* (2022) 11830–11837, <https://doi.org/10.1021/acscatal.2c03264>.
- F. Luo, L. Guo, Y. Xie, J. Xu, K. Qu, Z. Yang, Iridium nanorods as a robust and stable bifunctional electrocatalyst for pH-universal water splitting, *Appl. Catal. B Environ.* 279 (2020) 119394–119404, <https://doi.org/10.1016/j.apcatb.2020.119394>.
- Y. Gu, A. Wu, Y. Jiao, H. Zheng, X. Wang, Y. Xie, L. Wang, C. Tian, H. Fu, Two-dimensional porous molybdenum phosphide/nitride heterojunction nanosheets for pH-universal hydrogen evolution reaction, *Angew. Chem. Int. Ed.* 60 (2021) 6673–6681, <https://doi.org/10.1002/anie.202016102>.
- R. Zhang, X. Wang, S. Yu, T. Wen, X. Zhu, F. Yang, X. Sun, X. Wang, W. Hu, Ternary NiCo₂Px nanowires as pH-Universal electrocatalysts for highly efficient hydrogen evolution reaction, *Adv. Mater.* 29 (2017) 1605502–1605507, <https://doi.org/10.1002/adma.201605502>.
- Q. Li, X. Zou, X. Ai, H. Chen, L. Sun, X. Zou, Revealing activity trends of metal diborides toward pH-universal hydrogen evolution electrocatalysts with Pt-like activity, *Adv. Energy Mater.* (2018) 1803369–1803376, <https://doi.org/10.1002/aenm.201803369>.
- L. Wang, X. Duan, X. Liu, J. Gu, R. Si, Y. Qiu, Y. Qiu, D. Shi, F. Chen, X. Sun, J. Lin, J. Sun, Atomically dispersed Mo supported on metallic Co₉S₈ nanoflakes as an advanced noble-metal-free bifunctional water splitting catalyst working in universal pH conditions, *Adv. Energy Mater.* 10 (2020) 1903137–1903140, <https://doi.org/10.1002/aenm.201903137>.
- M. Kim, M.A.R. Anjum, M. Choi, H.Y. Jeong, S.H. Choi, N. Park, J.S. Lee, Covalent 0D–2D heterostructuring of Co₉S₈–MoS₂ for enhanced hydrogen evolution in all pH electrolytes, *Adv. Funct. Mater.* 30 (2020) 2002536–2002546, <https://doi.org/10.1002/adfm.202002536>.
- T. Liu, P. Li, N. Yao, G. Cheng, S. Chen, W. Luo, Y. Yin, CoP-doped MOF-based electrocatalyst for pH-universal hydrogen evolution reaction, *Angew. Chem. Int. Ed.* 58 (2019) 4679–4684, <https://doi.org/10.1002/anie.201901409>.
- L. Liao, L. Yang, G. Zhao, H. Zhou, F. Cai, Y. Li, X. Wang, F. Yu, Boosting pH-universal hydrogen evolution of molybdenum disulfide particles by interfacial engineering, *Chin. J. Chem.* 39 (2021) 288–294, <https://doi.org/10.1002/cjoc.202000487>.
- J. Zhang, Z. Zhang, Y. Ji, J. Yang, K. Fan, X. Ma, C. Wang, R. Shu, Y. Chen, Surface engineering induced hierarchical porous Ni₁₂P₅–Ni₂P polymorphs catalyst for efficient wide pH hydrogen production, *Appl. Catal. B Environ.* 282 (2021) 119609–119620, <https://doi.org/10.1016/j.apcatb.2020.119609>.
- C. Hong, X. Li, W. Wei, X. Wu, Q. Zhu, Nano-engineering of Ru-based hierarchical porous nanoreactors for highly efficient pH-universal overall water splitting, *Appl. Catal. B Environ.* 294 (2021) 120230–120243, <https://doi.org/10.1016/j.apcatb.2021.120230>.
- F. Yang, Y. Zhao, Y. Du, Y. Chen, G. Cheng, S. Chen, W. Luo, A monodisperse Rh₂P-Based electrocatalyst for highly efficient and pH-Universal hydrogen evolution reaction, *Adv. Energy Mater.* 8 (2018) 1703489–1703496, <https://doi.org/10.1002/aenm.201703489>.
- X. Mu, J. Gu, F. Feng, Z. Xiao, C. Chen, S. Liu, S. Mu, RuRh bimetallic nanoring as high-efficiency pH-universal catalyst for hydrogen evolution reaction, *Adv. Sci.* 8 (2021) 2002341–2002348, <https://doi.org/10.1002/advs.202002341>.
- W. Yu, H. Huang, Y. Qin, D. Zhang, Y. Zhang, K. Liu, Y. Zhang, J. Lai, L. Wang, The synergistic effect of pyrrolic-N and pyridinic-N with Pt under strong metal-support interaction to achieve high-performance alkaline hydrogen evolution, *Adv. Energy Mater.* 12 (2022) 2200110–2200117, <https://doi.org/10.1002/aenm.202200110>.
- Y. Huang, X. Mao, G. Yuan, D. Zhang, B. Pan, J. Deng, Y. Shi, N. Han, C. Li, L. Zhang, L. Wang, L. He, Y. Li, Y. Li, Size-dependent selectivity of electrochemical CO₂ reduction on converted In₂O₃ nanocrystals, *Angew. Chem. Int. Ed.* 60 (2021) 15844–15848, <https://doi.org/10.1002/anie.202105256>.
- T. Cui, J. Chi, J. Zhu, X. Sun, J. Lai, Z. Li, L. Wang, Tuning the size and chemisorption of Fe₄⁺ by trace Ru doping for hydrazine-assisted hydrogen evolution in seawater at large-current-density, *Appl. Catal. B Environ.* 319 (2022) 121950–121959, <https://doi.org/10.1016/j.apcatb.2022.121950>.
- X. Wu, W. Xu, Z. Wang, H. Li, M. Wang, D. Zhang, J. Lai, L. Wang, Rapid microwave synthesis of Ru-supported partially carbonized conductive metal-organic framework for efficient hydrogen evolution, *Chem. Eng. J.* 431 (2022) 133247–133255, <https://doi.org/10.1016/j.cej.2021.133247>.
- C. Li, J. Zhao, L. Xie, J. Wu, G. Li, Water adsorption and dissociation promoted by Co²⁺–N–C⁶⁰–Biactive sites of metallic Co/N-Doped carbon hybrids for efficient hydrogen evolution, *Appl. Catal. B Environ.* 282 (2021) 119463–119472, <https://doi.org/10.1016/j.apcatb.2020.119463>.
- M. Zhang, Q. Dai, H. Zheng, M. Chen, L. Dai, Novel MOF-derived Co@N-C bifunctional catalysts for highly efficient Zn-air batteries and water splitting, *Adv. Mater.* 30 (2018) 1705431–1705440, <https://doi.org/10.1002/adma.201705431>.
- L. Zhang, T. Gu, K. Lu, L. Zhou, D. S. Li, R. Wang, Engineering synergistic edge-N dipole in metal-free carbon nanoflakes toward intensified oxygen reduction electrocatalysis, *Adv. Funct. Mater.* 31 (2021) 2103187–2103195, <https://doi.org/10.1002/adfm.202103187>.
- N. Logeshwaran, S. Ramakrishnan, S.S. Chandrasekaran, M. Vinothkannan, A. R. Kim, S. Sengodan, D.B. Velusamy, P. Varadhan, J. He, D.J. Yoo, An efficient and durable trifunctional electrocatalyst for zinc-air batteries driven overall water splitting, *Appl. Catal. B Environ.* 297 (2021) 120405–120416, <https://doi.org/10.1016/j.apcatb.2021.120405>.
- Y. Wang, W. Guo, Z. Zhu, K. Xu, H. Zhang, W. Wei, X. Xiao, W. Liang, M. He, T. Yu, D. Zhang, H. Zhao, X. Xu, T. Yang, Interfacial boron modification on mesoporous octahedral rhodium shell and its enhanced electrocatalysis for water splitting and oxygen reduction, *Chem. Eng. J.* 435 (2022), 134982, <https://doi.org/10.1016/j.cej.2022.134982>.
- H. Sun, W. Zhang, J. Li, Z. Li, X. Ao, K. Xue, K.K. Ostrikov, J. Tang, C. Wang, Rh-engineered ultrathin NiFe-LDH nanosheets enable highly-efficient overall water splitting and urea electrolysis, *Appl. Catal. B Environ.* 284 (2021) 119740–119751, <https://doi.org/10.1016/j.apcatb.2020.119740>.
- K. Deng, Q. Mao, W. Wang, P. Wang, Z. Wang, Y. Xu, X. Li, H. Wang, L. Wang, Defect-rich low-crystalline Rh metallene for efficient chlorine-free H₂ production

by hydrazine-assisted seawater splitting, *Appl. Catal. B Environ.* 310 (2022) 121338–121346, <https://doi.org/10.1016/j.apcatb.2022.121338>.

[35] Y. Qiao, P. Yuan, C. Pao, Y. Cheng, Z. Pu, Q. Xu, S. Mu, J. Zhang, Boron-rich environment boosting ruthenium boride on B, N doped carbon outperforms platinum for hydrogen evolution reaction in a universal pH range, *Nano Energy* 75 (2020) 104881–104889, <https://doi.org/10.1016/j.nanoen.2020.104881>.

[36] A. Wang, C. Zhao, M. Yu, W. Wang, Trifunctional Co nanoparticle confined in defect-rich nitrogen-doped graphene for rechargeable Zn-air battery with a long lifetime, *Appl. Catal. B Environ.* 281 (2021) 119514–119523, <https://doi.org/10.1016/j.apcatb.2020.119514>.

[37] A.B. Anderson, T.V. Albu, Ab initio determination of reversible potentials and activation energies for Outer-sphere oxygen reduction to water and the reverse oxidation reaction, *J. Am. Chem. Soc.* 121 (1999) 11855–11863, <https://doi.org/10.1021/ja992735d>.

[38] Y. Li, J. Zhang, Y. Liu, Q. Qian, Z. Li, Y. Zhu, G. Zhang, Partially exposed RuP₂ surface in hybrid structure endows its bifunctionality for hydrazine oxidation and hydrogen evolution catalysis, *Adv. Sci.* 6 (2020) eabb4197, <https://doi.org/10.1126/sciadv.abb4197>.

[39] J. Jiang, S. Bai, M. Yang, J. Zou, N. Li, J. Peng, H. Wang, K. Xiang, S. Liu, T. Zhai, Strategic design and fabrication of MXenes-Ti₃CNCl₂@CoS₂ core-shell nanostructure for high-efficiency hydrogen evolution, *Nano Res.* 15 (2022) 5977–5986, <https://doi.org/10.1007/s12274-022-4276-8>.

[40] Y. Liu, J. Zhang, Y. Li, Q. Qian, Z. Li, Y. Zhu, G. Zhang, Manipulating dehydrogenation kinetics through dual-doping Co₃N electrode enables highly efficient hydrazine oxidation assisting self-powered H₂ production, *Nat. Commun.* 11 (2020) 1853–1865, <https://doi.org/10.1038/s41467-020-15563-8>.

[41] C. Li, H. Jang, S. Liu, M.G. Kim, L. Hou, X. Liu, J. Cho, P and Mo dual doped Ru ultrasmall nanoclusters embedded in P-doped porous carbon toward efficient hydrogen evolution reaction, *Adv. Energy Mater.* (2022) 2200029–2200037, <https://doi.org/10.1002/aenm.202200029>.

[42] Y. Liu, J. Zhang, Y. Li, Q. Qian, Z. Li, G. Zhang, Realizing the synergy of interface engineering and chemical substitution for Ni₃N enables its bifunctionality toward hydrazine oxidation assisted energy-saving hydrogen production, *Adv. Funct. Mater.* 31 (2021) 2103673–2103683, <https://doi.org/10.1002/adfm.202103673>.